Ultrafast charge migration in tyrosine and tryptophan: Branch energy bias and aromatic ring participation

Wan-Dong Yu(于皖东), Zhi-Han Huan(宦芷函), Zhi-Hong Yang(杨志红), Yu Zhang(张煜), Yun-Hui Wang(王允辉)

Citation: Chin. Phys. B. 35, 108201 (2026). DOI: 10.1088/1674-1056/ae74bf | CSTR: 32038.14.CPB.ae74bf

http://cpb.iphy.ac.cn; http://iopscience.iop.org/cpb

What follows is a list of articles you may be interested in

Effects of π-conjugation-substitution on ESIPT process for oxazoline-substituted hydroxyfluorenes

Di Wang(汪迪), Qiao Zhou(周悄), Qiang Wei(魏强), Peng Song(宋朋)

Chin. Phys. B. 32, 028201 (2023). DOI: 10.1088/1674-1056/ac65f4

Theoretical study on the mechanism for the excited-state double proton transfer process of an asymmetric Schiff base ligand

Zhengran Wang(王正然), Qiao Zhou(周悄), Bifa Cao(曹必发), Bo Li(栗博), Lixia Zhu(朱丽霞), Xinglei Zhang(张星蕾), Hang Yin(尹航), Ying Shi(石英)

Chin. Phys. B. 31, 048202 (2022). DOI: 10.1088/1674-1056/ac21c2

A DFT/TD-DFT study of effect of different substituent on ESIPT fluorescence features of 2-(2'-hydroxyphenyl)-4-chloro- methylthiazole derivatives

Shen-Yang Su(苏申阳), Xiu-Ning Liang(梁秀宁), Hua Fang(方华)

Chin. Phys. B. 31, 038202 (2022). DOI: 10.1088/1674-1056/ac21c6

Influence of intramolecular hydrogen bond formation sites on fluorescence mechanism

Hong-Bin Zhan(战鸿彬), Heng-Wei Zhang(张恒炜), Jun-Jie Jiang(江俊杰), Yi Wang(王一), Xu Fei(费旭), Jing Tian(田晶)

Chin. Phys. B. 31, 038201 (2022). DOI: 10.1088/1674-1056/ac29ad

Relationship between ESIPT properties and antioxidant activities of 5-hydroxyflavone derivates

Chaofan Sun(孙朝范), Bifa Cao(曹必发), Hang Yin(尹航), Ying Shi(石英)

Chin. Phys. B. 29, 058202 (2020). DOI: 10.1088/1674-1056/ab7ea1

Ultrafast charge migration in tyrosine and tryptophan: Branch energy bias and aromatic ring participation

Wan-Dong Yu(于皖东)[1], Zhi-Han Huan(宦芷函)[2], Zhi-Hong Yang(杨志红)[2], Yu Zhang(张煜)[3,†], and Yun-Hui Wang(王允辉)[2,‡]

[1] *Frontier Innovation Center for Structure and Dynamics of Matter, School of Science, Nanjing University of Posts and Telecommunications, Nanjing* 210023, *China*

[2] *New Energy Technology Engineering Laboratory of Jiangsu Province, Information Physics Research Center, School of Science, Nanjing University of Posts and Telecommunications, Nanjing* 210023, *China*

[3] *College of Mechanical Engineering, Jiaxing University, Jiaxing* 314001, *China*

(Received 17 March 2026; revised manuscript received 12 May 2026; accepted manuscript online 29 May 2026)

We investigate ultrafast hole migration in the amino acids tyrosine and tryptophan after strong-field ionization. The initial junction-localized hole state is prepared using constrained density functional theory, and its subsequent dynamics are followed using time-dependent density functional theory. In the time domain, both molecules show delayed but finite involvement of the aromatic unit, with a much shorter timescale for aromatic engagement in tryptophan (Trp) than in tyrosine (Tyr). Frequency-domain analysis reveals distinct beating energies associated with long-distance hole redistribution between the branch and the ring. These features can be understood within a simplified two-level Rabi picture, which captures the dominant peaks in the hole dynamics. We further show that the constrained density functional theory (cDFT) site-energy landscape connects the energetics of initial hole localization to the subsequent quantum-beat signatures: in both molecules, the terminal oxygen on the functional branch is the energetically favored hole site, explaining the initial tendency of a junction-launched hole to move toward the branch. Our results may provide a practical framework for interpreting and potentially controlling ultrafast charge migration in complex molecules.

Keywords: ultrafast charge migration, time-dependent density functional theory, constrained density functional theory, strong-field ionization

PACS: 82.39.Jn, 34.70.+e, 33.20.Xx

DOI: 10.1088/1674-1056/ae74bf **CSTR:** 32038.14.CPB.ae74bf

1. Introduction

With the development of advanced laser techniques, measurements of ultrafast processes have entered the attosecond regime, i.e., the natural timescale of electronic motion within molecules.[1–3] This progress has pushed molecular science beyond conventional photochemistry and opened the possibility of preparing coherent electronic excitations, forming localized electronic wave packets, and steering their interference to influence chemical reactivity.[4] In this context, ultrafast charge migration (UCM) triggered by strong-field ionization (SFI) has attracted growing interest.[5,6] UCM refers to the motion of charge, either an electron or a hole, on a subfemtosecond to few-femtosecond timescale after sudden ionization, usually before nuclear motion becomes important.[7–9] Because it occurs before significant structural rearrangement, UCM is closely linked to the attosecond control of charge-driven reactivity.[10,11]

Extending time-resolved studies of UCM to polyatomic molecules is a major goal of attochemistry, although techniques that combine attosecond resolution with complex molecular targets are still at an early stage. To the best of our knowledge, the first pump–probe measurements of UCM in molecules using isolated attosecond pulses were reported for H_2 and D_2 in 2010.[12] For polyatomic molecules, UCM had already been proposed by Cederbaum and Zobeley,[13] but a direct experimental demonstration was not achieved until 2014.[14] Since then, subfemtosecond electronic dynamics has been observed in several organic molecules, from small species[15,16] to larger biomolecules.[17–22]

The physics of UCM is rich and complex because it depends on several coupled factors,[23–25] including the initial state, the local chemical environment, functional groups, and many-electron correlations. As a result, its mechanisms remain incompletely understood.[26] When nuclear motion is neglected, theoretical studies have shown that UCM can be driven purely by electronic correlations in biomolecules.[27–33] Proposed mechanisms include the ultrafast response of electrons to the exchange-correlation hole,[34] the initial-state population effect,[35] π-bond-mediated hopping,[36] and quantum beating.[37]

A central issue in these studies is how to describe the hole created by SFI. In many works, ionization is modeled

†Corresponding author. E-mail: zyclay@outlook.com

‡Corresponding author. E-mail: yhwang@njupt.edu.cn

© 2026 Chinese Physical Society and IOP Publishing Ltd. All rights, including for text and data mining, AI training, and similar technologies, are reserved.

as the sudden removal of electrons from selected occupied orbitals, leaving *in situ* holes in the molecular cation whose subsequent evolution is driven by electronic correlations. In this picture, the predicted UCM depends strongly on the initially ionized orbital, which determines the initial hole distribution and its coupling to other cationic states. More recently, constrained density functional theory (cDFT) has been proposed as a practical way to describe the initial hole distribution produced by SFI.[38] It has been shown that cDFT-generated initial hole states can yield more realistic charge dynamics than the sudden removal of electrons from occupied Kohn–Sham orbitals (KSOs).[39] In addition, cDFT allows one to prepare a localized hole distribution and is especially useful when ionization is expected to occur near electron-rich functional groups after SFI.[12,14] This cDFT-based initialization has provided a multi-orbital perspective on UCM, including long-range charge migration,[40] attosecond molecular modes,[41] and particle-like hole propagation.[42,43]

In this paper, we extend the study of UCM to two amino acids, tryptophan ($C_{11}H_{12}N_2O_2$, Trp) and tyrosine ($C_9H_{11}NO_3$, Tyr), after SFI. We focus on the case in which the initial hole is localized in the junction region between the functional branch and the aromatic ring, with its density centered on the N atom. To model this situation, we initialize a unit hole in this junction region using cDFT and then follow its time evolution using time-dependent density functional theory (TDDFT).[44] Our study is motivated by three questions: if a localized hole is created in this branch–ring junction region, will it move first toward the functional branch or toward the aromatic ring, and what determines this preference? Does the resulting UCM exhibit a distinct dynamical mechanism? Can Trp and Tyr, which share the same branch composition, $-C_3H_6NO_2$, but differ strongly in the topology of their aromatic units, provide a useful platform for understanding how molecular structure shapes UCM?

The rest of this paper is organized as follows. First, we briefly introduce the cDFT and TDDFT frameworks and give the key computational parameters, whose convergence has been verified. Next, we discuss the UCM of Trp and Tyr in the coordinate and frequency domains and compare the two systems in detail. Finally, we present our conclusions.

2. Methodology

The initial site-specific hole density created by SFI is modeled using constrained density functional theory (cDFT),[38,39] which has proven to be a useful method in electronic-structure calculations. cDFT can help overcome some limitations in (TD)DFT, such as the inaccurate description of long-range charge transfer and excited-state electron transfer.[45] Analogous to Refs. [41,42,46], we assume that a coordinate-dependent constraint is applied to the many-electron system. This constraint forces the electronic density into a spatial distribution different from that of the unconstrained system. The constraint condition is usually written as follows:

$$\int w(\boldsymbol{r})\rho(\boldsymbol{r})\,\mathrm{d}\boldsymbol{r} - F = 0, \tag{1}$$

where $w(\boldsymbol{r})$ is the weight function, $\rho(\boldsymbol{r})$ is the electronic density, and F is the constraint value. In the Kohn–Sham (KS) formalism, one solves the following cDFT self-consistent equation

$$H_\mathrm{c}\psi_i(\boldsymbol{r}) = \varepsilon_i\psi_i(\boldsymbol{r}). \tag{2}$$

The constrained Hamiltonian H_c consists of the standard KS Hamiltonian H_KS and an external constraint potential $\lambda w(\boldsymbol{r})$

$$H_\mathrm{c} = H_\mathrm{KS} + \lambda w(\boldsymbol{r}), \tag{3}$$

where λ is the Lagrangian multiplier, and H_KS includes the kinetic term, the nuclear potential, the Hartree potential, and the exchange-correlation potential

$$H_\mathrm{KS} = -\frac{\nabla^2}{2} + v_n + \int \frac{\rho(\boldsymbol{r}')}{|\boldsymbol{r}-\boldsymbol{r}'|}d\boldsymbol{r}' + v_{xc}(\boldsymbol{r}). \tag{4}$$

By solving Eq. (2) self-consistently together with Eq. (1), one obtains both λ and the cDFT ground-state KSOs ψ_i, while ensuring that the constraint is satisfied.[47–49] The resulting KSOs ψ_i provide the initial state with a localized hole on a selected atomic site. In the present work, cDFT is not used as a replacement for real-time TDDFT. Rather, it is used only as an initial-state preparation tool. The constraint potential $\lambda w(\boldsymbol{r})$ prepares a cationic state with a unit hole localized around the selected atom. After convergence of this constrained state, $\lambda w(\boldsymbol{r})$ is switched off, and the system is propagated under the ordinary unconstrained TDDFT Hamiltonian H_KS. Thus, the calculated dynamics correspond to the field-free evolution of a localized-hole wavepacket prepared by cDFT.

All calculations are performed using the OCTOPUS program, where cDFT has been implemented for finite systems.[46,50] Numerical quantities are represented on a real-space grid in a box of $52 \times 52 \times 48$ a_0^3 with a uniform spacing of 0.27 a_0. The adiabatic local-density approximation is employed.[51] Core electrons are described by norm-conserving pseudopotentials.[52] The weight function $w(\boldsymbol{r})$ is defined using the Hirshfeld partition scheme[49]

$$w(\boldsymbol{r}) = \frac{\sum_{I\in D}\rho^I(\boldsymbol{r}-\boldsymbol{R}_I) - \sum_{I\in A}\rho^I(\boldsymbol{r}-\boldsymbol{R}_I)}{\sum_I \rho^I_\sigma(\boldsymbol{r}-\boldsymbol{R}_I)}, \tag{5}$$

where $\rho^I_\sigma(\boldsymbol{r}-\boldsymbol{R}_I)$ denotes the free-atom ground-state electronic density of the Ith atom at the distance $\boldsymbol{r}$ from the atomic position $\boldsymbol{R}_I$. D is the electron-donor region, related to the specific atom that constrains the hole density. A is the acceptor region, the complementary region of D. The nuclei are kept fixed at the ground-state equilibrium geometry of the neutral

molecule. In TD calculations, the time-evolution operator is approximated using the enforced time-reversal symmetry algorithm, with a fixed time step of 6.04×10^{-3} fs.[53,54] The total propagation time is 12 fs. A Gaussian-windowed Fourier transform is used to extract the frequency spectrum of hole oscillation. Atomic units are used unless otherwise stated.

To ensure that the reported UCM modes are not artifacts of the numerical setup, representative convergence tests were performed for the parameters most directly affecting the real-time propagation and Fourier analysis. The electronic time step and real-space grid spacing were varied, and the resulting dipole spectra and space-frequency maps were compared with those obtained using the production parameters. The dominant spectral peaks and the qualitative spatial distributions of the corresponding hole oscillation modes were unchanged within the numerical resolution. The Fourier-processing procedure was also checked by varying the Gaussian-window parameters.

It is emphasized that the fixed-nuclei approximation is used here to isolate the primary electronic component of UCM. This approximation is appropriate for the early-time regime of charge migration, which typically occurs on a few-femtosecond timescale after sudden ionization and before substantial nuclear rearrangement. Previous studies have shown that nuclear motion has little influence on the charge-migration dynamics during the first several femtoseconds.[19,32] In the present systems, the dominant modes around 1–2 eV correspond to oscillation periods of roughly 2–4 fs, so the main features analyzed here lie on the electronic timescale. We therefore regard the present simulations as representing the fixed-geometry electronic limit of UCM. Including nuclear motion would be expected to modulate the electronic oscillations, leading to effects such as vibrational sidebands,[50] decoherence,[31] and recoherence.[55]

In this paper, the three-dimensional (3D) hole density $\rho^H(\boldsymbol{r},t)$ is defined as the difference between the electronic density of the neutral ground state, $\rho^0(\boldsymbol{r})$, and that of the cation, $\rho^+(\boldsymbol{r},t)$: $\rho^H(\boldsymbol{r},t) = \rho^0(\boldsymbol{r}) - \rho^+(\boldsymbol{r},t)$. Since neither Tyr nor Trp is planar, we choose the xy plane to better visualize the hole-density distribution, as shown in Fig. 1. Most features of UCM can be identified in this plane, while the variation along the z direction is relatively minor. For this reason, we further define the one-dimensional (1D) integrated hole densities along the x and y axes as $\rho^h(x,t) = \int \rho^H(x,y,z,t)\,\mathrm{d}y\mathrm{d}z$ and $\rho^h(y,t) = \int \rho^H(x,y,z,t)\,\mathrm{d}x\mathrm{d}z$, respectively.

For space-frequency maps, the position-resolved hole-density signals contain spatial components that contribute strongly near zero frequency. Therefore, for position-resolved frequency signals, for example, in Fig. 3(a), the time-averaged component at each spatial coordinate was removed before Fourier transformation

$$S(x,\Omega) = \int_0^T [\rho^h(x,t) - \frac{1}{T}\int_0^T \rho^h(x,t)\,\mathrm{d}t]G(t)\,\mathrm{e}^{\mathrm{i}\Omega t}\,\mathrm{d}t, \quad (6)$$

where $S(x,\Omega)$ is the Fourier amplitude. $G(t)$ is a Gaussian window function used to reduce finite-time boundary effects, centered at 6 fs with a standard deviation of 1.8 fs. Ω is the angular frequency. The plotted space-frequency intensity is then proportional to $|S(x,\Omega)|^2$. Subtracting the time-averaged component is a standard preprocessing step in Fourier analysis for signals containing a large static background. It does not change the dominant finite-frequency UCM peaks or their spatial assignments. It only suppresses the static and near-zero-frequency background, making the finite-frequency charge-migration modes more clearly visible. This mean-subtraction procedure was used only for the position-resolved maps and not for the dipole spectra. For the dipole spectra, the calculated raw time-dependent dipole moment $d_\alpha(t)$, where $\alpha = x,y,z$, was Fourier transformed directly using the same $G(t)$.

3. Results and discussion

As shown in Fig. 1, for both Trp and Tyr, a unit hole created by SFI is initially localized on the junction N_a atom. Since the two molecules have the same side-branch composition, we use the same labels for the branch atoms, N_a and O_a. For the aromatic part, we use different labels, e.g., N_b for Trp and O_b for Tyr.

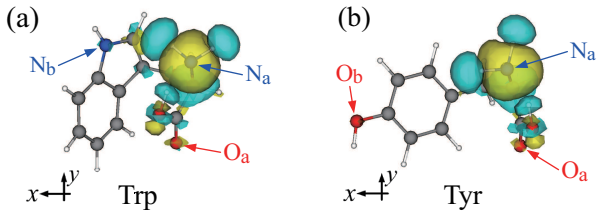

Fig. 1. Initial cDFT hole density $\rho^H(\boldsymbol{r},t=0)$ with a unit hole constrained on N_a. Golden and cyan isosurfaces denote positive and negative hole densities, with fixed isovalues of 0.01 and -0.01 a_0^{-3}, respectively. Nuclei are shown as balls of different sizes and colors: H (white), N (blue), C (gray), and O (red). The corresponding Lagrange multipliers λ for Trp and Tyr are 0.77 and 0.78 a.u., respectively.

To gain insight into UCM, we first examine the dynamics in Trp and then compare them with those in Tyr. As shown in Fig. 2(a), the 1D integrated hole density of bicyclic Trp along the x axis, $\rho^h(x,t)$, exhibits three main features. First, before about 2 fs, most of the hole density remains on the branch, while only a small fraction reaches the far side of the aromatic ring, as indicated by the hole density near C_a, which serves as a clear reference point. Second, before about 2 fs, a small region of negative hole density (brown) appears in the junction region near $x = 0$, indicating the formation of an effective barrier in the connecting region between the branch and the ring. The same barrier feature can also be seen in the 3D hole-density

plots of the junction carbons at 0.5 fs, as shown in the insets. Third, after about 2 fs, the negative hole density in the junction region spreads out. The positive hole density then extends over the molecular skeleton and starts to oscillate between the branch and C_a.

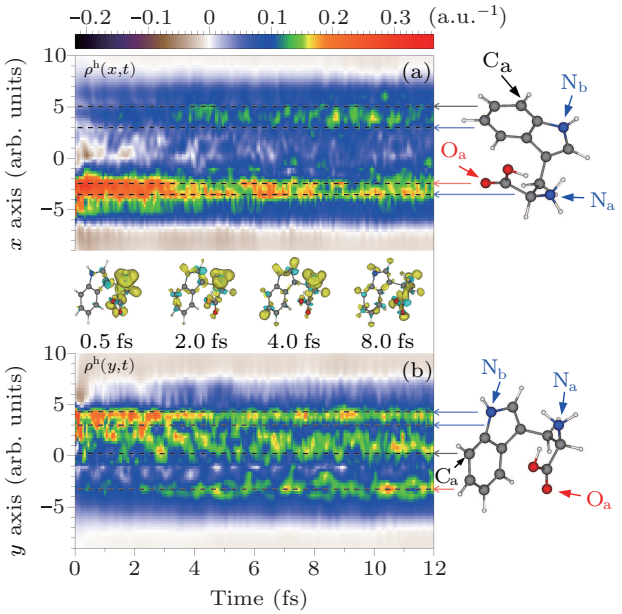

Fig. 2. Time evolution of the 1D integrated hole densities (a) $\rho^h(x,t)$ and (b) $\rho^h(y,t)$ for Trp. Middle panels: 3D hole density $\rho^H(\boldsymbol{r},t)$ at representative time instants. Horizontal dashed lines and arrows are included to guide the eye.

It is also instructive to examine the UCM along the y direction. Figure 2(b) shows that the hole density $\rho^h(y,t)$ rapidly leaves N_a along the y axis, allowing part of the hole density to reach O_a within 0.5 fs. At later times, the hole oscillates between the two terminal regions along the y axis. Together with the results in Fig. 2(a), this shows that in Trp, the hole first oscillates rapidly within the branch during the first 2 fs and then spreads across the entire molecular skeleton, leading to terminal-to-terminal oscillation in the xy plane.

To clarify the UCM in the frequency domain, we extract frequency maps along different axes, as shown in Fig. 3. Overall, the main frequencies lie below 7 eV, consistent with the excitation energy of the cDFT initial state and thus with the strength of the external constraint applied to the molecule. Although the maps in Figs. 3(a) and 3(b) appear complicated, three main features can be identified. First, the peaks at 1.05 eV and 5.33 eV, which are the largest and second-largest peaks in Fig. 3(c), correspond to long-range UCM between different atomic sites. These frequencies persist because the oscillation phases from different spatial regions add constructively rather than cancel. Second, Fig. 3(a) shows that the 1.05 eV mode is associated with hole oscillation between C_a and the branch, whereas the 5.33 eV mode is mainly associated with oscillation within the branch. Third, the local minimum at 2.87 eV mainly arises from local modes concentrated near individual nuclei, whose oscillation phases largely cancel each other.

Next, we analyze UCM in Tyr for comparison. Unlike Trp, Tyr contains only a single aromatic ring. Although its side branch has the same chemical formula as that of Trp, its spatial arrangement differs. As in Trp, we first constrain a unit hole on N_a and then examine the resulting UCM in both the coordinate and frequency domains.

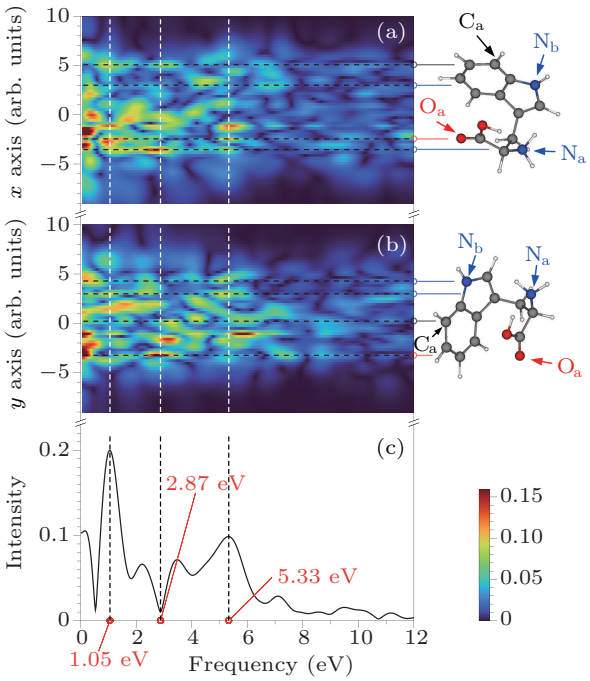

Fig. 3. Frequency analysis of UCM in Trp for an initial hole localized at N_a. (a) Space-frequency distribution of the hole density along the x axis. (b) Same as in (a), but along the y axis. (c) Frequency spectrum of the hole dipole moment along the x axis. Vertical dashed lines mark the largest peak, the second-largest peak, and a local minimum. Horizontal dashed lines are included to guide the eye.

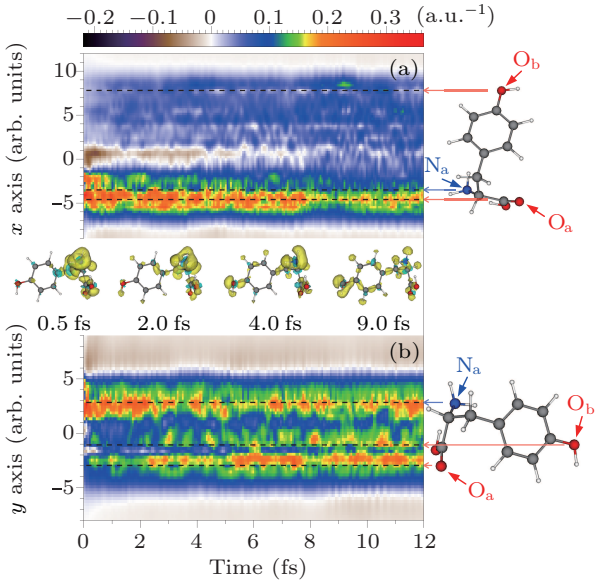

Fig. 4. Time evolution of the 1D integrated hole densities (a) $\rho^h(x,t)$ and (b) $\rho^h(y,t)$ for Tyr. Middle panels: 3D hole density $\rho^H(\boldsymbol{r},t)$ at representative time instants. Horizontal dashed lines and arrows are included to guide the eye.

As shown in Fig. 4(a), before about 4 fs, the hole density $\rho^h(x,t)$ in Tyr exhibits a more pronounced negative region (brown) in the junction region near $x = 0$. During this stage, less hole density migrates into the aromatic ring than in Trp. Together with Fig. 4(b), this indicates that the hole can move along the entire y direction without encountering a clear negative-hole-density confinement or barrier. At about 9 fs, the hole density along the x axis spreads across the entire molecular skeleton and reaches the terminal O_b, as also shown in the middle 3D hole-density plot. Therefore, in Tyr, a hole initially localized on N_a takes longer to reach the terminal site on the aromatic ring, and UCM across the entire molecule begins later than in Trp.

We also analyze the space-frequency maps and the frequency spectrum of the hole dipole moment along the x direction for Tyr. As shown in Fig. 5, most of the hole oscillation frequencies lie below 7 eV, similar to the case of Trp. The peak at 0.98 eV is associated with long-range hole migration from O_a on the branch to O_b at the end of the aromatic ring, and it corresponds to the largest peak in the hole dipole spectrum. The 1.90 eV mode is mainly associated with oscillation within the branch, especially between O_a and N_a, and contributes the second-largest peak. In contrast, the local minimum at 5.88 eV mainly arises from local UCM modes whose oscillation phases largely cancel each other. These local modes are distributed along the entire carbon skeleton, as seen in both the x and y directions.

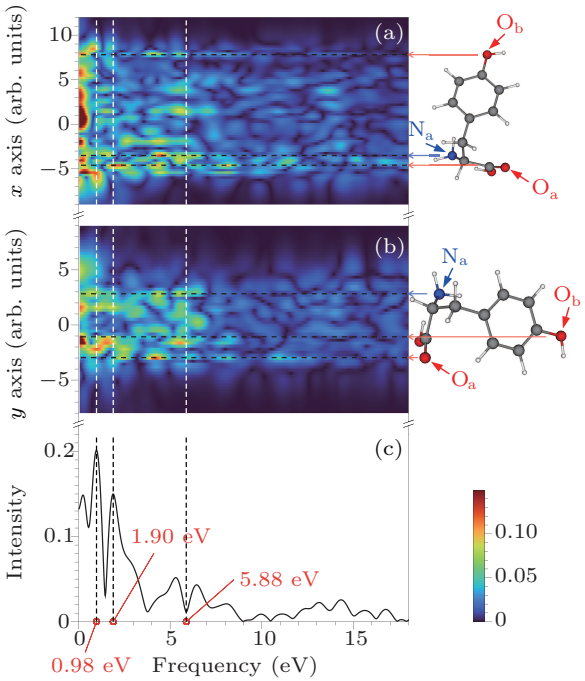

Fig. 5. Frequency analysis of UCM in Tyr for an initial hole localized at N_a. (a) Space-frequency distribution of the hole density along the x axis. (b) Same as in (a), but along the y axis. (c) Frequency spectrum of the hole dipole moment along the x axis. Vertical dashed lines mark the largest peak, the second-largest peak, and a local minimum. Horizontal dashed lines are included to guide the eye.

The above frequency analysis shows that both Trp and Tyr exhibit clear low-frequency modes around 1 eV. These modes are associated with long-range UCM between the terminal functional group on the branch and the ring. Compared with Trp, Tyr exhibits stronger low-frequency excitation, as indicated by the more prominent low-frequency region in Fig. 5(c). In addition, the 1.90 eV mode mainly reflects coherent UCM within the branch, further suggesting a higher optical susceptibility of the Tyr branch. We assign the 1.90 eV mode primarily to coherent UCM for the following reason: the 1.90 eV mode appears at several positions along the functional branch as the same well-defined finite-frequency mode. We therefore attribute it to a collective branch-local oscillation between N_a and O_a rather than to independent local fluctuations. Here, "coherent" means that these spatial regions participate in a single phase-correlated hole-beating mode, analogous to a normal mode of coupled classical oscillators.

To clarify the microscopic mechanism of UCM, we calculate the off-diagonal density-matrix elements of the outermost π-like KSOs, denoted by $\overline{M}$, as shown in Fig. 6. The upper panels display these off-diagonal elements under the constrained Hamiltonian H_c. They show how the KSOs respond to the constraint potential λw. For Trp, shown in the left column of Fig. 6(a), the values of $\overline{M}$ indicate that H_c strongly mixes several initial KSOs and generates substantial coherence among them. This suggests that the potential λw plays an important role in reshaping the cationic eigensystem. The distribution of the off-diagonal strengths shows that the largest responses occur for the 6th, 7th, 9th, and 10th orbitals, indicating that the strongest coherence mainly involves these four orbitals. Since the subsequent time propagation is performed with H_{KS}, the beating frequencies generated by the initial cDFT state ψ_i can be approximately analyzed within a two-level Rabi picture,[56] that is, by decomposing the UCM into coupled two-orbital contributions. We further calculate that the Rabi frequency between the 6th and 7th orbitals is 0.17 eV, while that between the 7th and 9th orbitals is 0.85 eV. Their sum, 1.02 eV, is close to the strongest peak at 1.05 eV in Fig. 3(c), suggesting that this peak mainly arises from quantum beating involving the 6th and 9th KSOs. The lower panels show the initial cDFT orbitals ψ_i together with the corresponding DFT orbitals of the cationic ground state. The DFT orbitals are the eigenstates of H_{KS} with the largest projection overlaps with ψ_i. As indicated by the red arrows, the potential λw spatially distorts the cationic DFT orbitals, transforming them into the cDFT orbitals.

We perform the same analysis for Tyr, which has fewer outermost KSOs than Trp. The corresponding off-diagonal elements are shown in Fig. 6(b). Similar behavior is observed in Tyr: the 4th, 5th, and 6th orbitals are the most sensitive to the

potential λw. It should be noted that the 1st to 3rd KSOs are π-like orbitals mainly localized on the branch and therefore do not contribute to the long-range peaks seen in Fig. 5(c). Using the two-level Rabi approximation, we find that the beating frequency between the 4th and 5th orbitals is 0.30 eV, while that between the 5th and 6th orbitals is 0.66 eV. Their sum is 0.96 eV, which is very close to the largest peak at 0.98 eV in Fig. 5(c). This suggests that the largest peak is mainly associated with quantum beating involving the 4th and 6th orbitals. For both Trp and Tyr, the spatial distributions of the initial cDFT ground-state KSOs, ψ_i, reveal an interesting feature. The 7th orbital in Trp and the 5th orbital in Tyr may serve as bridge orbitals, with their densities distributed over both the aromatic ring and the branch.

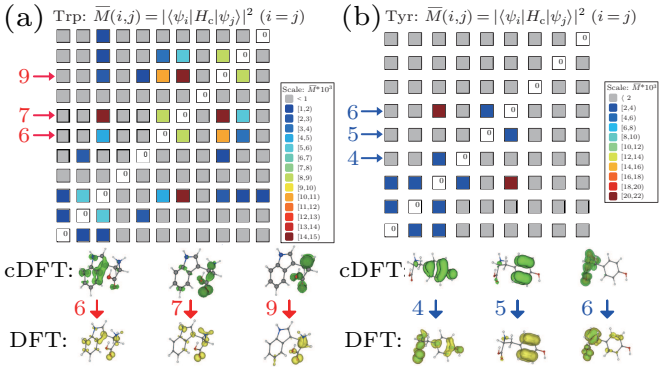

Fig. 6. KSO coherence induced by the initial constrained Hamiltonian H_c for (a) Trp and (b) Tyr. Top: off-diagonal density-matrix elements for the outermost π-like orbitals. The diagonal elements are omitted and set to zero. Bottom: 3D KSOs relevant to UCM for the initial constrained state (labeled as cDFT) and the cationic ground state (labeled as DFT). Vertical arrows indicate the cationic ground-state orbitals with the largest projection overlaps.

To gain further insight into the initial direction of hole flow, especially within the first 2 fs, we use the cDFT site-energy landscape as a reference, as shown in Fig. 7. The site energy of each atom is obtained from the self-consistent cDFT total energy with a unit hole constrained on that atom. For example, in Fig. 7(a), the site energy of N_b (1.98 eV) is defined as the total-energy difference between the cDFT state with the hole constrained on N_b and that with the hole constrained on N_a. This site-energy landscape helps us understand the initial preference of a hole localized on N_a. In Fig. 7(a), the site energy of O_a is much lower than that of N_a, indicating that the hole can move rapidly from N_a to the branch site. In this sense, O_a acts as an energy well with a stronger hole affinity than N_b. At the same time, the site energy of N_b is close to that of N_a, suggesting that the hole-localized states on these two nitrogen sites are nearly resonant. This near resonance may therefore facilitate early transfer of hole density from N_a to the ring.

We emphasize that this near-resonance is not the fundamental source of coherence. Coherence is generated by the removal of the cDFT constraint, which leaves the system in a non-stationary electronic state that evolves under the constraint-free H_{KS}. In the two-state picture, the near-resonance between N_a- and N_b-localized hole configurations instead reduces the detuning between these diabatic states and can therefore enhance the amplitude of coherent hole transfer. In this sense, the cDFT site-energy landscape serves as a static guide to hole affinity and preferred migration pathways. The actual oscillation frequencies and mode amplitudes are determined by the TDDFT evolution and the orbital couplings discussed in Fig. 6.

For Tyr, the corresponding cDFT site-energy landscape is shown in Fig. 7(b). Taking the N_a-constrained cDFT state as the zero reference, the site energies of O_a and O_b are -13.28 and -9.75 eV, respectively. These values indicate that the initially prepared N_a-localized hole is energetically unstable with respect to transfer to the oxygen-centered sites. Since O_a is the lowest-energy site and lies on the functional branch, the early-time dynamics is dominated by hole motion from N_a toward O_a. Thus, the branch-local N_a–O_a oscillation is retained, consistent with the 1.90 eV mode in Fig. 5, which mainly reflects coherent UCM within the branch.

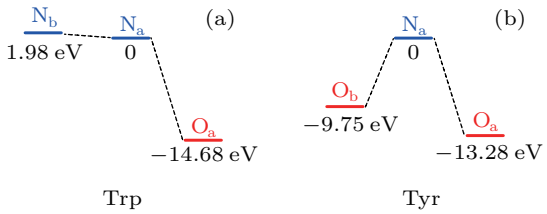

Fig. 7. cDFT site-energy landscapes for (a) Trp and (b) Tyr. The plotted value at atom X is defined as $\Delta E_X = E_{cDFT}(X) - E_{cDFT}(N_a)$, where $E_{cDFT}(X)$ is the self-consistent cDFT total energy with a unit hole constrained on atom X. The N_a-constrained cDFT state is therefore taken as the zero reference, $\Delta E_{N_a} = 0$. Negative values indicate atoms that are more favorable for hole localization than N_a.

The delayed migration to O_b should therefore be understood as a later-stage process rather than as a direct early transfer from N_a to the ring. In contrast to Trp, Tyr does not possess a ring site close in energy to N_a that can act as a near-resonant partner for immediate transfer from the initially constrained site. After the cDFT constraint is removed, however, the initial state evolves under the field-free KS Hamiltonian into a coherent wavepacket involving several KS components. Within this evolving wavepacket, the relevant long-range channel involves O_a and O_b. Because O_b is much closer in cDFT site energy to O_a than to N_a, the site-energy landscape provides a qualitative explanation for why the later branch-to-ring oscillation becomes energetically favorable. This interpretation is consistent with the delayed appearance of hole density near O_b at around 9 fs in Fig. 4(a) and with the 0.98 eV mode in Fig. 5, which is assigned to long-range migration between O_a and O_b.

4. Conclusion

Within the cDFT and TDDFT framework, we studied UCM triggered by SFI in two amino acids, Trp and Tyr. These two molecules share a similar side branch with the same chemical formula but differ in their aromatic-ring structures. This makes them a useful pair for comparison and for understanding the mechanism of UCM. By constraining a unit hole in the junction region centered on the N_a atom, we find that the hole density first moves to the branch and then oscillates throughout the molecule. The hole migration exhibits two main types of characteristic frequencies. One corresponds to long-range modes, in which the hole oscillates between the terminal functional groups on the branch and the ring. The other corresponds to local modes, which contribute only weakly to the hole dipole moment. Furthermore, within a two-level Rabi picture, the largest peaks in both Trp and Tyr can be traced to several key orbitals identified from the density-matrix elements under the constrained Hamiltonian H_c. In addition, the cDFT site-energy landscape provides a useful reference for understanding the initial direction of hole flow in complex molecules. Our study may provide a practical and predictive framework for identifying where a suddenly created hole is likely to localize and the femtosecond timescale over which it can spread to, or remain confined within, aromatic and functional regions. This may help interpret and eventually control UCM in complex molecules.

Acknowledgments

Project supported by the National Natural Science Foundation of China (Grant Nos. 12104019 and 12104185), the Natural Science Foundation of Jiangsu Province (Grant No. BK20253027), and the Natural Science Research Start-up Foundation of Recruiting Talents of Nanjing University of Posts and Telecommunications (Grant No. NY223203). YZ thanks the Jiaxing Young Sci-Tech Talent Special Program (Grant No. 2024AY40007).

References

[1] Krausz F and Ivanov M 2009 *Rev. Mod. Phys.* **81** 163
[2] Nisoli M, Decleva P, Calegari F, Palacios A and Martín F 2017 *Chem. Rev.* **117** 10760
[3] Kraus P M, Zürch M, Cushing S K, Neumark D M and Leone S R 2018 *Nat. Rev. Chem.* **2** 82
[4] Alexander O, Ayuso D, Matthews M, Rego L, Tisch J, Weaver B and Marangos J 2025 *Appl. Phys. Lett.* **126**
[5] Peng P, Marceau C and Villeneuve D M 2019 *Nat. Rev. Phys.* **1** 144
[6] He L, Sun S, Lan P, He Y, Wang B, Wang P, Zhu X, Li L, Cao W, Lu P and Lin C D 2022 *Nat. Commun.* **13** 4595
[7] Golubev N V, Begušić T and Vaníček J 2020 *Phys. Rev. Lett.* **125** 083001
[8] Arnold C, Vendrell O and Santra R 2017 *Phys. Rev. A* **95** 033425
[9] Despré V, Golubev N V and Kuleff A I 2018 *Phys. Rev. Lett.* **121** 203002
[10] Goulielmakis E, Loh Z H, Wirth A, Santra R, Rohringer N, Yakovlev V S, Zherebtsov S, Pfeifer T, Azzeer A M, Kling M F, Leone S R and Krausz F 2010 *Nature* **466** 739
[11] Kling M F, von den Hoff P, Znakovskaya I and de Vivie-Riedle R 2013 *Phys. Chem. Chem. Phys.* **15** 9448
[12] Sansone G, Kelkensberg F, Pérez-Torres J F, Morales F, Kling M F, Siu W, Ghafur O, Johnsson P, Swoboda M, Benedetti E, Ferrari F, Lépine F, Sanz-Vicario J L, Zherebtsov S, Znakovskaya I, L'Huillier A, Ivanov M Y, Nisoli M, Martín F and Vrakking M J J 2010 *Nature* **465** 763
[13] Cederbaum L S and Zobeley J 1999 *Chem. Phys. Lett.* **307** 205
[14] Calegari F, Ayuso D, Trabattoni A, Belshaw L, De Camillis S, Anumula S, Frassetto F, Poletto L, Palacios A, Decleva P, Greenwood J B, Martín F and Nisoli M 2014 *Science* **346** 336
[15] Kraus P M, Mignolet B, Baykusheva D, Rupenyan A, Horný L, Penka E F, Grassi G, Tolstikhin O I, Schneider J, Jensen F, Madsen L B, Bandrauk A D, Remacle F and Wörner H J 2015 *Science* **350** 790
[16] He L, He Y, Sun S, Goetz E, Le A T, Zhu X, Lan P, Lu P and Lin C D 2023 *Adv. Photon.* **5** 056001
[17] Ayuso D, Palacios A, Decleva P and Martín F 2017 *Phys. Chem. Chem. Phys.* **19** 19767
[18] Grell G, Guo Z, Driver T, Decleva P, Plésiat E, Picón A, González-Vázquez J, Walter P, Marangos J P, Cryan J P, Marinelli A, Palacios A and Martín F 2023 *Phys. Rev. Res.* **5** 023092
[19] Månsson E P, Latini S, Covito F, Wanie V, Galli M, Perfetto E, Stefanucci G, Hübener H, De Giovannini U, Castrovilli M C, Trabattoni A, Frassetto F, Poletto L, Greenwood J B, Légaré F, Nisoli M, Rubio A and Calegari F 2021 *Commun. Chem.* **4** 73
[20] Lara-Astiaso M, Galli M, Trabattoni A, Palacios A, Ayuso D, Frassetto F, Poletto L, De Camillis S, Greenwood J, Decleva P, Tavernelli I, Calegari F, Nisoli M and Martín F 2018 *J. Phys. Chem. Lett.* **9** 4570
[21] Renaud N, Harris M A, Singh A P, Berlin Y A, Ratner M A, Wasielewski M R, Lewis F D and Grozema F C 2016 *Nat. Chem.* **8** 1015
[22] Vismarra F, Fernández-Villoria F, Mocci D, González-Vázquez J, Wu Y, Colaizzi L, Holzmeier F, Delgado J, Santos J, Bañares L, Carlini L, Castrovilli M C, Bolognesi P, Richter R, Avaldi L, Palacios A, Lucchini M, Reduzzi M, Borrego-Varillas R, Martín N, Martín F and Nisoli M 2024 *Nat. Chem.* **16** 2017
[23] Kuleff A I and Cederbaum L S 2014 *J. Phys. B:At., Mol. Opt. Phys.* **47** 124002
[24] Ponseca Jr C S, Chábera P, Uhlig J, Persson P and Sundstrom V 2017 *Chem. Rev.* **117** 10940
[25] Wörner H J, Arrell C A, Banerji N, Cannizzo A, Chergui M, Das A K, Hamm P, Keller U, Kraus P M, Liberatore E, Lopez-Tarifa P, Lucchini M, Meuwly M, Milne C J, Moser J-E, Rothlisberger U, Smolentsev G, Teuscher J, van Bokhoven J A and Wenger O S 2017 *Struct. Dyn.* **4** 061508
[26] Calegari F and Martin F 2023 *Commun. Chem.* **6** 184
[27] Lünnemann S, Kuleff A I and Cederbaum L S 2008 *Chem. Phys. Lett.* **450** 232
[28] Kuleff A I, Lünnemann S and Cederbaum L S 2013 *Chem. Phys.* **414** 100
[29] Vacher M, Bearpark M J and Robb M A 2014 *J. Chem. Phys.* **140** 201102
[30] Calegari F, Ayuso D, Trabattoni A, Belshaw L, De Camillis S, Frassetto F, Poletto L, Palacios A, Decleva P, Greenwood J B, *et al.* 2015 *IEEE J. Sel. Top. Quantum Electron.* **21** 8700512
[31] Lara-Astiaso M, Ayuso D, Tavernelli I, Decleva P, Palacios A and Martín F 2016 *Faraday Discuss.* **194** 41
[32] Polyak I, Jenkins A J, Vacher M, Bouduban M E, Bearpark M J and Robb M A 2018 *Mol. Phys.* **116** 2474
[33] Khalili F, Vafaee M, Cho D and Shokri B 2021 *Int. J. Quantum Chem.* **121**
[34] Breidbach J and Cederbaum L 2005 *Phys. Rev. Lett.* **94** 033901
[35] Bruner A, Hernandez S, Mauger F, Abanador P M, LaMaster D J, Gaarde M B, Schafer K J and Lopata K 2017 *J. Phys. Chem. Lett.* **8** 3991
[36] Dutoi A D, Wormit M and Cederbaum L S 2011 *J. Chem. Phys.* **134** 024303
[37] Breidbach J and Cederbaum L 2003 *J. Chem. Phys.* **118** 3983
[38] Kaduk B, Kowalczyk T and Van Voorhis T 2012 *Chem. Rev.* **112** 321
[39] Eshuis H and Van Voorhis T 2009 *Phys. Chem. Chem. Phys.* **11** 10293
[40] Folorunso A S, Mauger F, Hamer K A, Jayasinghe D D, Wahyutama I S, Ragains J R, Jones R R, DiMauro L F, Gaarde M B, Schafer K J and Lopata K 2023 *J. Phys. Chem. A* **127** 1894

[41] Folorunso A S, Bruner A, Mauger F, Hamer K A, Hernandez S, Jones R R, DiMauro L F, Gaarde M B, Schafer K J and Lopata K 2021 *Phys. Rev. Lett.* **126** 133002
[42] Hamer K A, Mauger F, Folorunso A S, Lopata K, Jones R R, DiMauro L F, Schafer K J and Gaarde M B 2022 *Phys. Rev. A* **106** 013103
[43] Mauger F, Folorunso A S, Hamer K A, Chandre C, Gaarde M B, Lopata K and Schafer K J 2022 *Phys. Rev. Res.* **4** 013073
[44] Runge E and Gross E K U 1984 *Phys. Rev. Lett.* **52** 997
[45] Wu Q and Van Voorhis T 2006 *J. Chem. Theory Comput.* **2** 765
[46] Yu W D, Liang H, Geng L and Peng L Y 2023 *Phys. Rev. A* **107** 013101
[47] Wu Q and Van Voorhis T 2005 *Phys. Rev. A* **72** 024502
[48] O'Regan D D and Teobaldi G 2016 *Phys. Rev. B* **94** 035159
[49] Kidd D, Umar A S and Varga K 2018 *Phys. Rev. B* **98** 075108
[50] Yu W D, Geng L and Peng L Y 2023 *Phys. Rev. A* **108** 062807
[51] Perdew J P and Zunger A 1981 *Phys. Rev. B* **23** 5048
[52] Hartwigsen C, Goedecker S and Hutter J 1998 *Phys. Rev. B* **58** 3641
[53] Gomez Pueyo A, Marques M A, Rubio A and Castro A 2018 *J. Chem. Theory Comput.* **14** 3040
[54] Neufeld O, Zhang J, De Giovannini U, Hübener H and Rubio A 2022 *Proc. Natl. Acad. Sci.* **119** e2204219119
[55] Matselyukh D T, Despré V, Golubev N V, Kuleff A I and Wörner H J 2022 *Nat. Phys.* **18** 1206
[56] Knight P L and Milonni P W 1980 *Phys. Rep.* **66** 21